A robust GNSS/INS integrated system for pedestrian navigation in urban environments based on spatial consistency check

Xiaoji Niu, Zhihao Liu, Longyang Ding, and Jian Kuang

***Abstract*—Pedestrian navigation using smart devices has become increasingly prevalent in daily life. Typically, the user's location in outdoor environments can be obtained via the embedded global navigation satellite system (GNSS) chip. However, in urban environments, the performance of conventional GNSS positioning is significantly degraded due to multipath effects and non-line-of-sight (NLOS) receptions that ruin the GNSS observations. To address this challenge, this paper proposes a robust GNSS/inertial navigation system (INS) integrated system for pedestrian navigation in urban environments. Based on robust optimization algorithm, the proposed method utilizes the spatial consistency between multi-epoch GNSS pseudorange observations and pedestrian dead reckoning (PDR) trajectory to detect GNSS outliers. Then, the fault-free GNSS observations are integrated with INS-based PDR via the conventional robust Kalman filter (RKF) in tightly-coupled mode. To validate the performance of the proposed method, nine sets of test data were collected covering three typical urban scenarios. Experimental results show that the proposed method achieves an average horizontal positioning accuracy of 10.21 m (95%), compared to 17.27 m for the conventional RKF, representing an improvement of approximately 41%.**

***Index Terms*—Pedestrian navigation, global navigation satellite system (GNSS)/inertial navigation system (INS) integration, spatial consistency check, GNSS outlier detection, robust optimization.**

I. INTRODUCTION

LOCATION-based services (LBS) have brought great convenience to daily life [1], which enable personal localization and real-time navigation. Generally, smart devices such as smartphones and smartwatches serve as the primary platforms for providing LBS, and three principal approaches have been adopted. The first utilizes the low-cost global navigation satellite system (GNSS) chip to determine the user's location in outdoor environments [2]. The second relies on wireless signals such as Wi-Fi and Bluetooth to identify the user's position in indoor environments [3]. The third approach is known as pedestrian dead reckoning (PDR), which just relies on the built-in inertial measurement unit (IMU) [4]. In practical applications, PDR is usually integrated with the other two methods to achieve higher positioning accuracy.

In current stage, GNSS is the most commonly used approach for pedestrian navigation using smart devices. Generally, GNSS chips can provide satisfactory solutions in open-sky environments. However, as urban activity intensifies, GNSS positioning in dense cityscapes faces increasing challenges [5]. In complex urban environments, multipath effects and non-line-of-sight (NLOS) receptions caused by high-raise buildings and other obstructions severely ruin the GNSS observations, causing final performance significantly degraded, even to an unacceptable level [6]. Consequently, extensive research has been devoted to detecting and mitigating GNSS outliers under these conditions, which is precisely the challenge this paper aims to address.

A. Outlier Detection for GNSS Positioning

For GNSS positioning, various techniques have been developed to detect and mitigate observation outliers. Receiver autonomous integrity monitoring (RAIM) is a classical fault detection and exclusion (FDE) algorithm that has been widely applied in GNSS positioning [7]. It works based on consistency check among redundant range measurements and assumes that only a single fault exists, which significantly limits its effectiveness in urban environments where multiple faults simultaneously occur [8]. To address this limitation, advanced RAIM (ARAIM) with multiple hypothesis solution separation (MHSS) algorithm has been proposed, which allows multiple faults detection and exclusion [9]. Moreover, Yang and Xu [10] introduced a robust-estimation-based RAIM, which can process multiple constellations and multiple outliers. In contrast to RAIM-based approaches, Wen et al. [11] utilized random sample consensus (RANSAC) to mitigate multiple outliers, and the core principle remains rooted in consistency check. Despite the effectiveness of the mentioned methods, it remains a challenge for them to be applied in the conditions where the number of redundant fault-free observations are insufficient, particularly in urban environments.

Additionally, environmental sensing has emerged as an effective strategy for GNSS outlier detection [12]. For

This work was supported in part by the Hubei Provincial Natural Science Foundation Program under Grant 2023AFB021, in part by the Fundamental Research Funds for the Central Universities under Grant 2042023kf0124. (*Corresponding author: Jian Kuang.*)

Xiaoji Niu, Zhihao Liu, Longyang Ding, and Jian Kuang are with the GNSS Research Center, Wuhan University, Wuhan 430072, China. Xiaoji Niu and Jian Kuang are also with the Hubei Technology Innovation Center for Spatiotemporal Information and Positioning Navigation, Wuhan 430072, China. Zhihao Liu and Longyang Ding are also with the School of Geodesy and Geomatics, Wuhan University, Wuhan 430072, China (e-mail: xjniu@whu.edu.cn; zhihao.liu@whu.edu.cn; dingly@whu.edu.cn; kuang@whu.edu.cn).

instance, Wang et al. [13] proposed a shadow matching approach, which utilizes a three-dimensional (3D) city model to enhance urban positioning accuracy. Furthermore, Bai et al. [14] employed a sky-pointing fish-eye camera to identify and exclude NLOS receptions. El-Mowafy et al. [15] introduced a novel approach for integrity monitoring by combining ARAIM and 3D city models. More recently, Weng et al. [16] proposed a sidewalk matching technique for pedestrian navigation in urban canyons. This technique does not rely on 3D building models, but a simple pedestrian map and smartphone sensors (i.e., accelerometer and gyroscope) are needed. A common limitation of these methods is the reliance on additional environment information, which may not be readily available or convenient to obtain.

B. Outlier Detection for GNSS/INS Integrated Positioning

In addition to GNSS positioning, GNSS/inertial navigation system (INS) integration has been a promising solution for pedestrian navigation [17]. On the one hand, fusion algorithms help mitigate the impact of GNSS outliers on positioning accuracy. On the other hand, in some areas where GNSS signals are not available, the integrated system can still work for a period of time. Nevertheless, GNSS outlier detection remains essential to ensure reliable positioning performance in complex urban environments.

For the fusion algorithm, Kalman filter (KF) has been widely used [18]. To mitigate GNSS outliers, robust KF (RKF) with M-estimation is one of the classical methods [19]. The robust chi-square test method (RCTM) is another classical approach that detects GNSS outliers by using innovation vector generated in filtering process [20]. Moreover, RANSAC algorithm has been adopted in tightly-coupled GNSS/INS integration [21]. Since only two fault-free satellites are screened out, the iteration number of this algorithm is greatly reduced. Besides abrupt faults, slow growing error (SGE) also need to be considered in KF model [22]. Generally, an approach known as autonomous integrity monitoring by extrapolation (AIME) is used to detect SGE, which relies on multi-epoch innovation vectors and corresponding covariance matrices [23]. More recently, Jiang et al. [24] proposed an enhanced AIME algorithm, and the difference is that the test statistics for each satellite are calculated individually, which means that the faulty satellites can be more easily identified in tightly-coupled mode.

Besides KF-based fusion algorithm, GNSS/INS integration using factor graph optimization (FGO) has been widely investigated in recent years. The differences between the FGO and KF approaches are that the KF has lower computational load, while FGO benefits from the ability to leverage historical data. Sunderhauf et al. [25] introduced the robust optimization from simultaneous localization and mapping (SLAM) to GNSS multipath mitigation problem. In this approach, GNSS-based localization is modelled as factor graphs and solved using nonlinear least square methods. Then, a comprehensive comparison between FGO and extended KF (EKF) has been conducted [26]. It is concluded that the FGO-based sensor fusion performs better than that of EKF in both loosely-coupled and tightly-coupled mode, but the drawback is that FGO leads to a greater computational load as all historical data are used. Furthermore, an approach known as graduated non-convexity (GNC) [27] is introduced to FGO for GNSS outlier mitigation, and a coarse-to-fine approach is proposed to eliminate the need for an accurate initial guess [12]. More relevantly, IMU-based PDR/GNSS integration via FGO has been implemented on smartphones [28], [29], and a walking gaits aided method is adopted to suppress pseudorange outliers [30].

According to the literature review, KF-based framework is more suitable for smart devices due to lower computational load. However, FGO-based methods demonstrate that GNSS outlier detection can be effectively improved by using historical data. Therefore, a hybrid approach that combines the respective advantages of both methods is proposed in this paper. In brief, historical measurements are utilized for GNSS outlier detection; then, the detected satellites are discarded in the KF-based GNSS/INS integration. In this paper, the use of historical data for GNSS outlier detection is termed spatial consistency check. This method is based on the fact that the changes in multi-epoch GNSS pseudorange observations should correspond to the variations of pedestrian's spatial position. Conversely, when the changes are inconsistent with the historical trajectory, the corresponding satellite is likely to be faulty.

Specifically, the proposed algorithm consists of three steps. First, based on the relative PDR trajectory formed from the IMU measurements, a lightweight robust optimization algorithm is designed to estimate the absolute historical trajectory. Then, the optimized results are used for GNSS outlier detection by performing the spatial consistency check. Finally, the fault-free GNSS observations are integrated with INS-based PDR via the conventional RKF in tightly-coupled mode.

The remainder of this paper is organized as follows: Section II introduces the methodologies of the proposed method. Section III describes the GNSS/INS integration via EKF in detail. Section IV interprets experimental setup. Section V and Section VI present test results and discussions, respectively. Section VII summaries the proposed method and outlines future works.

II. GNSS Outlier Detection Based on Spatial Consistency Check

In this section, the principles of the proposed method are described in detail, which consists of three parts. First, the conventional PDR algorithm is introduced. Then, a sliding-window-based robust optimization algorithm is designed, which converts the relative PDR trajectory into an absolute trajectory. Finally, the core idea of GNSS outlier detection using spatial consistency check is illustrated.

A. PDR Trajectory Generation

The conventional PDR algorithm consists of three modules, namely, step detection, step length estimation, and

pedestrian heading estimation. Generally, the accelerometer is used for step detection, and the norm of three-axis measurements is adopted as a detection feature [31]:

$$a_{norm} = \sqrt{a_x^2 + a_y^2 + a_z^2} \tag{1}$$

where a_x , a_y , and a_z represent the tri-accelerometer measurements. The signal peak or valley of the accumulated features within the detection window is identified as a step [32]. For step length estimation, an empirical formula is typically used [33]. Additionally, pedestrian heading estimation is a key factor that determines PDR performance, which can be provided by INS-based PDR and will be described in Section III. After completing the three steps, the PDR trajectory can be expressed as:

$$\begin{cases} X_{pdr}^{k+1} = X_{pdr}^{k} + SL_{k+1} \cdot \cos\varphi \\ Y_{pdr}^{k+1} = Y_{pdr}^{k} + SL_{k+1} \cdot \sin\varphi \end{cases} \tag{2}$$

where X and Y represent the north and east positions in the local-frame; SL and φ denote the step length and pedestrian heading, respectively; the superscript k denotes the step number. The initial position (X_{pdr}^{0} and Y_{pdr}^{0}) is set to 0.

However, it should be noted that the time when a step detected (t_{step}) is usually not consistent with the GNSS sampling time (t_{gnss}). Thus, the position difference caused by time inconsistency requires additional consideration. In this paper, the PDR position at GNSS sampling time is obtained via the time-based linear interpolation, i.e.:

$$\begin{cases} X_{pdr}^{t_{gnss}} = \dfrac{t_{gnss} - t_{step}^{k}}{t_{step}^{k+1} - t_{step}^{k}} X_{pdr}^{t_{step}^{k+1}} + \dfrac{t_{step}^{k+1} - t_{gnss}}{t_{step}^{k+1} - t_{step}^{k}} X_{pdr}^{t_{step}^{k}} \\ Y_{pdr}^{t_{gnss}} = \dfrac{t_{gnss} - t_{step}^{k}}{t_{step}^{k+1} - t_{step}^{k}} Y_{pdr}^{t_{step}^{k+1}} + \dfrac{t_{step}^{k+1} - t_{gnss}}{t_{step}^{k+1} - t_{step}^{k}} Y_{pdr}^{t_{step}^{k}} \end{cases} \tag{3}$$

where t_{step}^{k} and t_{step}^{k+1} represent the time of two adjacent steps and $t_{step}^{k} < t_{gnss} < t_{step}^{k+1}$. Note that the trajectory obtained in this step is a relative PDR trajectory. To obtain the absolute historical trajectory, further processing using an optimization algorithm is required.

B. Optimization Algorithm

Generally, FGO-based approaches utilize sliding window to process multi-epoch observations and ensure real-time performance. However, one node in FGO requires multiple parameters to estimate, so the number of parameters grows with the sliding window size. In contrast, a lightweight optimization algorithm is proposed in this paper, and the relative position of each node in the sliding window is obtained from the PDR trajectory. Therefore, fewer parameters that need to be estimated and its number is always unchanged.

The relation between multi-epoch GNSS pseudorange observations and PDR trajectory is illustrated in Fig. 1. To establish a connection with the GNSS pseudorange observations, the relative PDR trajectory generated in previous step needs to be converted into an absolute trajectory. It can be observed from Fig. 1 that there is a position offset between the two trajectories, namely, dX and dY (dZ is not demonstrated in Fig. 1). In addition, there is a rotation angle that needs to be considered. On the one hand, the rotation angle can be used for heading initialization of INS. The proposed algorithm assumes the initial heading is equal to 0. Thus, the rotation angle shown in Fig. 1 represents the difference between the initial heading and the absolute heading. If this angle can be estimated, the heading can be compensated within the algorithm [34]. On the other hand, after heading initialization, the rotation angle can be used to compensate the heading errors of PDR trajectory introduced by INS-based PDR. Moreover, considering that the step length is estimated using an empirical model and cannot adapt to different users, the scale factor also needs to be taken into account. Within a short duration, it is assumed that the pedestrian walks on a flat surface, so the 3D coordinates of the absolute trajectory can be written as:

$$\begin{cases} X_k^A = X_0^A + \kappa(X_k^R \cos\theta - Y_k^R \sin\theta) \\ Y_k^A = Y_0^A + \kappa(X_k^R \sin\theta + Y_k^R \cos\theta) \\ Z_k^A = Z_0^A \end{cases} \tag{4}$$

where the superscript A and R denote the absolute and the relative coordinates, respectively; X_0^A , Y_0^A , and Z_0^A are the initial position of the absolute PDR trajectory; κ is the scale factor; θ is the rotation angle.

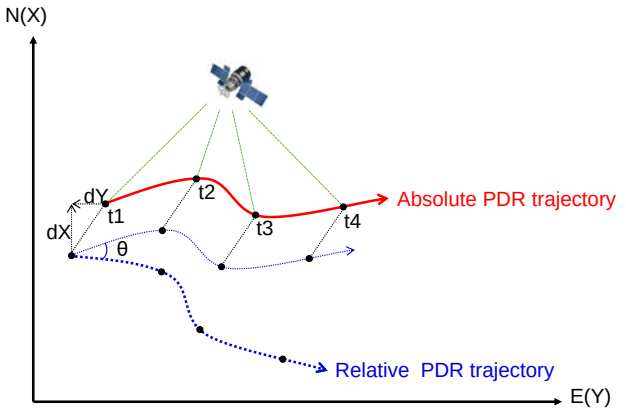

Fig. 1. The relation between multi-epoch GNSS pseudorange observations and PDR trajectory.

To estimate the parameters appearing in (4), a sliding-window-based optimization algorithm is designed here (20-second window size). According to the satellite positioning principles, the GNSS pseudorange observation can be expressed as:

$$\tilde{\rho}_k^j = \rho_k^j + c(\delta t_k^r - \delta t_k^j) + I_k^j + T_k^j + \varepsilon_{k,\rho}^j \tag{5}$$

where $\tilde{\rho}_k^j$ denotes the raw pseudorange observation in the *k*-th epoch of the *j*-th satellite; ρ_k^j is the geometric range from satellite to GNSS receiver; δt_k^r and δt_k^j are the clock bias of receiver and satellite, respectively; c is the speed of light; I_k^j and T_k^j represent the ionospheric and tropospheric delay in meter, respectively; $\varepsilon_{k,\rho}^j$ denotes the measurement noise and other

unmodeled errors, such as multipath effects and NLOS receptions.

As illustrated in Fig. 1, the pseudorange residual derived from the absolute PDR trajectory can be expressed as:

$$\begin{cases} \| e_{k,\rho}^{j} \|_{\sigma_{k,\rho}^{j}}^{2} = \| \overline{\rho}_{k}^{j} - h_{k,\rho}^{j}(\boldsymbol{p}_{k}^{j},\ \boldsymbol{p}_{k}^{r},\ \delta t_{k}^{r}) \|_{\sigma_{k,\rho}^{j}}^{2} \\ h_{k,\rho}^{j}(\boldsymbol{p}_{k}^{j},\ \boldsymbol{p}_{k}^{r},\ \delta t_{k}^{r}) = \| \boldsymbol{p}_{k}^{j} - \boldsymbol{p}_{k}^{r} \| + c \cdot \delta t_{k}^{r} \end{cases} \tag{6}$$

where $\overline{\rho}_{k}^{j}$ is the raw pseudorange observation that considering satellite clock bias and atmospheric effects elimination; $\boldsymbol{p}_{k}^{j}$ is the satellite position; $\boldsymbol{p}_{k}^{r} = (X_{k}^{A} \quad Y_{k}^{A} \quad Z_{k}^{A})^{T}$ is the receiver position provided by the absolute PDR trajectory; $\sigma_{k,\rho}^{j}$ is the standard deviation of pseudorange measurement, which can be modeled as:

$$(\sigma_{k,\rho}^{j})^{2} = (\sigma_{k,obs}^{j})^{2} + (\sigma_{k,eph}^{j})^{2} + (\sigma_{k,ion}^{j})^{2} + (\sigma_{k,trop}^{j})^{2} \tag{7}$$

where $\sigma_{k,obs}^{j}$, $\sigma_{k,eph}^{j}$, $\sigma_{k,eph}^{j}$, and $\sigma_{k,trop}^{j}$ are the standard deviation of measurement noise, satellite related errors, ionosphere error, and troposphere error, respectively.

In addition, to make use of GNSS Doppler observations, the average velocity of pedestrian can be calculated using the absolute PDR trajectory, i.e.:

$$\begin{cases} V_{X,t_{gnss}}^{A} = (X_{t_{step}^{k+1}}^{A} - X_{t_{step}^{k}}^{A})/dt \\ V_{Y,t_{gnss}}^{A} = (Y_{t_{step}^{k+1}}^{A} - Y_{t_{step}^{k}}^{A})/dt \\ V_{Z,t_{gnss}}^{A} = 0 \end{cases} \tag{8}$$

where $dt = t_{step}^{k+1} - t_{step}^{k}$ is the time interval between two adjacent steps. Then, the GNSS Doppler observation can be expressed as:

$$\tilde{D}_{k}^{j} = -\frac{1}{\lambda}\left(\boldsymbol{los}_{k}^{j}(\boldsymbol{v}_{k}^{j} - \boldsymbol{v}_{k}^{r}) + c\left(\dot{\delta}t_{k}^{r} - \dot{\delta}t_{k}^{j}\right)\right) + \varepsilon_{k,D}^{j} \tag{9}$$

where $\tilde{D}_{k}^{j}$ is the raw Doppler measurement; λ is the wavelength; $\boldsymbol{los}_{k}^{j}$ is the line-of-sight (LOS) unit vector from receiver to satellite; $\boldsymbol{v}_{k}^{j}$ is the satellite velocity; $\boldsymbol{v}_{k}^{r} = (V_{X,k}^{A} \quad V_{Y,k}^{A} \quad V_{Z,k}^{A})^{T}$ is the receiver velocity derived from the absolute PDR trajectory; $\dot{\delta}t_{k}^{r}$ and $\dot{\delta}t_{k}^{j}$ are the clock drift of receiver and satellite, respectively; $\varepsilon_{k,D}^{j}$ is the measurement noise. Finally, the Doppler residual can be formulated as:

$$\begin{cases} \| e_{k,D}^{j} \|_{\sigma_{k,D}^{j}}^{2} = \left\| \overline{D}_{k}^{j} - h_{k,D}^{j}\left(\boldsymbol{v}_{k}^{j},\ \boldsymbol{v}_{k}^{r},\ \dot{\delta}t_{k}^{r}\right) \right\|_{\sigma_{k,D}^{j}}^{2} \\ h_{k,D}^{j}\left(\boldsymbol{v}_{k}^{j},\ \boldsymbol{v}_{k}^{r},\ \dot{\delta}t_{k}^{r}\right) = -\frac{1}{\lambda}\left(\boldsymbol{los}_{k}^{j}(\boldsymbol{v}_{k}^{j} - \boldsymbol{v}_{k}^{r}) + c \cdot \dot{\delta}t_{k}^{r}\right) \end{cases} \tag{10}$$

where $\overline{D}_{k}^{j}$ is the raw Doppler observation that considering satellite clock drift elimination; $\sigma_{k,D}^{j}$ is the standard deviation of Doppler observation, which can be modeled as:

$$\sigma_{k,D}^{j} = \frac{1.0}{\sin(el_{k}^{j})} \tag{11}$$

where el_{k}^{j} is the corresponding elevation angle.

Furthermore, it is assumed that the clock drift is constant over the sliding window. Then, the receiver clock bias and clock drift can be modeled as:

$$\begin{cases} \delta t_{k}^{r} = \delta t_{0}^{r} + (t_{k} - t_{0}) \cdot \dot{\delta}t_{0}^{r} \\ \dot{\delta}t_{k}^{r} = \dot{\delta}t_{0}^{r} \end{cases} \tag{12}$$

where δt_{0}^{r} and $\dot{\delta}t_{0}^{r}$ are the clock bias and clock drift of the first epoch for the sliding window. Therefore, the state vector that needs to be estimated is written as:

$$\chi = \begin{bmatrix} X_{0}^{A} & Y_{0}^{A} & Z_{0}^{A} & \theta & \kappa & \delta t_{0}^{r} & \dot{\delta}t_{0}^{r} \end{bmatrix} \tag{13}$$

Finally, the objective function can be expressed as:

$$\chi^{*} = \arg\min_{\chi} \sum_{k=1}^{n} \sum_{j=1}^{m} \left(\| e_{k,\rho}^{j} \|_{\sigma_{k,\rho}^{j}}^{2} + \| e_{k,D}^{j} \|_{\sigma_{k,D}^{j}}^{2} \right) \tag{14}$$

However, in complex urban environments, the outliers in GNSS pseudorange observations need to be further considered in the optimization algorithm. A standard approach to address outliers is to use robust cost functions, i.e.:

$$\chi^{*} = \arg\min_{\chi} \sum_{k=1}^{n} \sum_{j=1}^{m} \left(L\left(\| e_{k,\rho}^{j} \|_{\sigma_{k,\rho}^{j}}^{2} \right) + L\left(\| e_{k,D}^{j} \|_{\sigma_{k,D}^{j}}^{2} \right) \right) \tag{15}$$

where $L(\cdot)$ denotes a robust cost function, and Huber loss function is used in this paper [35].

C. Spatial Consistency Check

Note that the positioning results can be obtained after performing the optimization algorithm. However, the influence of GNSS outliers on positioning performance cannot be completely eliminated. Since the optimization algorithm does not guarantee absolute positioning accuracy, a spatial consistency check is adopted, which focuses on the relative variations in the pedestrian's position.

For a given satellite across different epochs, the variations of GNSS pseudorange observations are associated with the changes of receiver's position. Therefore, in the sliding window, the pseudorange residuals calculated from the optimized results should remain roughly consistent in the conditions without GNSS outliers. The satellite with inconsistent residuals is more likely to be faulty, which is the core idea of the proposed spatial consistency check.

For the *j*-th satellite in the sliding window, the pseudorange residual is defined as:

$$\begin{cases} res_{t_1}^{j} = \overline{\rho}_{t_1}^{j} - \rho_{t_1,0}^{j} - \delta t_{1}^{r} \\ res_{t_2}^{j} = \overline{\rho}_{t_2}^{j} - \rho_{t_2,0}^{j} - \delta t_{2}^{r} \\ \cdots \\ res_{t_n}^{j} = \overline{\rho}_{t_n}^{j} - \rho_{t_n,0}^{j} - \delta t_{n}^{r} \end{cases} \tag{16}$$

where δt_{i}^{r} represents the clock bias that obtained from (12) and (15); $\rho_{t_i,0}^{j}$ is the geometric range from satellite to the optimized position:

$$\rho_{t_i,0}^{j} = \sqrt{(X_{t_i}^{A} - X_{t_i}^{j})^{2} + (Y_{t_i}^{A} - Y_{t_i}^{j})^{2} + (Z_{t_i}^{A} - Z_{t_i}^{j})^{2}} \tag{17}$$

Then, the spatial consistency check is performed and GNSS outlier can be judged through the formula:

$$\begin{cases} Max[\boldsymbol{res}] - Min[\boldsymbol{res}] > th1 \\ Std[\boldsymbol{res}] > th2 \end{cases} \tag{18}$$

where $Max[\cdot]$, $Min[\cdot]$, and $Std[\cdot]$ denote the maximum, minimum, and standard deviation function, respectively; $th1$ and $th2$ are two empirical thresholds set according to the measurement noise. For example, GNSS observations can be collected over a period of time in an open-sky environment to calculate the standard deviation (σ) of the pseudorange noise, which is then defined as $th2$. Subsequently, $th1$ can be set to four or six times $th2$ (i.e., $\pm 2\sigma$ or $\pm 3\sigma$). Specifically, the two thresholds are assigned with 6.0 and 1.5 in this paper, respectively.

III. GNSS/INS Integration

In this section, the system framework of the proposed algorithm is first introduced. Then, the detailed steps, including INS mechanization, filter design, pedestrian motion constraint, and tightly-coupled GNSS/INS integration, are described individually.

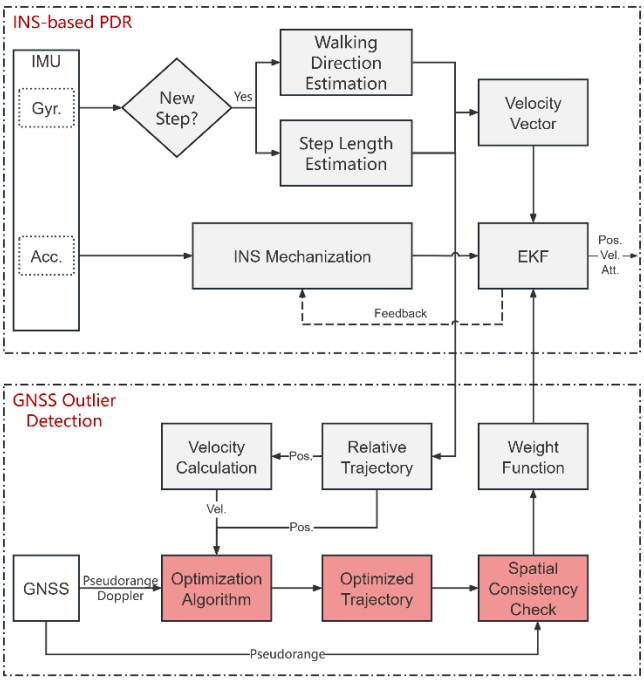

Fig. 2. System framework of the proposed method.

A. System Overview

The system framework of the proposed method is shown in Fig. 2, which adopts a conventional EKF framework to fuse GNSS observations and IMU measurements. The system consists of two parts: INS-based PDR and tightly-coupled GNSS/INS integration. INS-based PDR utilizes pedestrian motion constraint to improve the positioning performance. More important, it makes the navigation system can work in the area without GNSS signals. In addition, the key element, namely, PDR trajectory, is provided by this module. On the other hand, GNSS module also plays an important role in the algorithm framework, which provides absolute position information for the navigation system. Using classical RKF approaches, large-scale outliers are easy to detect, whereas small-scale outliers are more challenging to identify. The proposed method utilizes the characteristic that PDR can provide high precision positions in a short term to detect faulty satellites, which address this issue to a certain degree.

B. INS Mechanization

INS mechanization utilizes the specific force and angular rate measurements provided by the embedded accelerometer and gyroscope to provide continuous and high-frequency position, velocity, and attitude (PVA) results, which serves as the foundation of strap-down inertial navigation. After neglecting the small terms of error correction, the simplified form of INS mechanization is given as [36]:

$$\begin{pmatrix} \boldsymbol{r}_k^n \\ \boldsymbol{v}_k^n \\ \boldsymbol{C}_{b,k}^n \end{pmatrix} = \begin{pmatrix} \boldsymbol{r}_{k-1}^n + \boldsymbol{v}_k^n \Delta t \\ \boldsymbol{v}_{k-1}^n + \left[\boldsymbol{C}_{b,k}^n \left(\tilde{\boldsymbol{f}}_k^b - \boldsymbol{b}_a\right) + \boldsymbol{g}^n\right]\Delta t \\ \boldsymbol{C}_{b,k-1}^n + \boldsymbol{C}_{b,k-1}^n \Omega[(\tilde{\boldsymbol{\omega}}_k^b - \boldsymbol{b}_g)\Delta t] \end{pmatrix} \quad (19)$$

where $\boldsymbol{r}^n$ and $\boldsymbol{v}^n$ are the position and velocity vector in the navigation-frame (n-frame), respectively; $\boldsymbol{C}_b^n$ is the transformation matrix from the body-frame (b-frame) to the n-frame; $\tilde{\boldsymbol{f}}^b$ and $\tilde{\boldsymbol{\omega}}^b$ are the three-axis acceleration and angle rate measurements in the b-frame, respectively; $\boldsymbol{g}^n$ is the local gravity vector in the n-frame; $\boldsymbol{b}_a$ and $\boldsymbol{b}_g$ are the bias vector of the accelerometer and gyroscope, respectively; Δt is the time interval between two epochs; $\Omega[\cdot]$ denotes the cross-product form of a vector.

C. Filter Design

Since the error of INS can be rapidly accumulated in a few seconds when using the low-cost inertial sensors embedded in smart devices, EKF-based approaches are usually adopted to fuse INS with GNSS. Considering GPS and BDS, the 22-dimensional error state vector is defined as:

$$\delta\boldsymbol{x} = [\delta\boldsymbol{r}^n \quad \delta\boldsymbol{v}^n \quad \boldsymbol{\psi} \quad \delta\boldsymbol{b}_g \quad \delta\boldsymbol{b}_a \quad \delta\boldsymbol{l}^b \quad \delta\kappa \quad t_{bias}^g \quad t_{bias}^c \quad t_{drift}]^T \quad (20)$$

where $\delta\boldsymbol{r}^n$, $\delta\boldsymbol{v}^n$, and $\boldsymbol{\psi}$ represent the error vectors of position, velocity, and attitude in the n-frame, respectively; $\delta\boldsymbol{l}^b$ refers to the error vector of level-arm (from wrist to shoulder) in the b-frame, which is specifically design for swing mode; $\delta\kappa$ denotes the scale error; t_{bias}^g and t_{bias}^c denote the clock bias of GPS and BDS, respectively; t_{drift} is the clock drift. Then, the discrete linearization of the system error model can be expressed as:

$$\begin{cases} \delta\boldsymbol{x}_{k,k-1} = \boldsymbol{\Phi}_{k-1}\delta\boldsymbol{x}_{k-1,k-1} + \boldsymbol{\omega}_k \\ \delta\boldsymbol{z}_k = \boldsymbol{H}_k\delta\boldsymbol{x}_{k,k-1} + \boldsymbol{\varepsilon}_k \end{cases} \quad (21)$$

where $\delta\boldsymbol{x}_{k,k-1}$ is the predicted error state vector; $\delta\boldsymbol{x}_{k-1,k-1}$ represents the previous error state vector; $\delta\boldsymbol{z}_k$ is the measurement vector; $\boldsymbol{H}_k$ denotes the design matrix; $\boldsymbol{\omega}_k$ and $\boldsymbol{\varepsilon}_k$ are the process noise and measurement noise, respectively; $\boldsymbol{\Phi}_{k-1}$ is the 22×22 state transition matrix:

$$\boldsymbol{\Phi}_{k-1}=\begin{bmatrix}\boldsymbol{\Phi}_{k-1}^{ins} & \boldsymbol{O}\\ \boldsymbol{O} & \boldsymbol{\Phi}_{k-1}^{gnss}\end{bmatrix} \tag{22}$$

$$\boldsymbol{\Phi}_{k-1}^{ins}=\begin{bmatrix}\boldsymbol{I}_{3\times3} & \boldsymbol{I}_{3\times3}\Delta t & 0_{3\times3} & 0_{3\times3} & 0_{3\times3} & 0_{3\times4}\\ 0_{3\times3} & \boldsymbol{I}_{3\times3} & (\boldsymbol{f}_k^n\times)\Delta t & 0_{3\times3} & \boldsymbol{C}_{b,k}^n\Delta t & 0_{3\times4}\\ 0_{3\times3} & 0_{3\times3} & \boldsymbol{I}_{3\times3} & -\boldsymbol{C}_{b,k}^n\Delta t & 0_{3\times3} & 0_{3\times4}\\ 0_{3\times3} & 0_{3\times3} & 0_{3\times3} & \boldsymbol{I}_{3\times3} & 0_{3\times3} & 0_{3\times4}\\ 0_{3\times3} & 0_{3\times3} & 0_{3\times3} & 0_{3\times3} & \boldsymbol{I}_{3\times3} & 0_{3\times4}\\ 0_{4\times3} & 0_{4\times3} & 0_{4\times3} & 0_{4\times3} & 0_{4\times3} & \boldsymbol{I}_{4\times4}\end{bmatrix} \tag{23}$$

$$\boldsymbol{\Phi}_{k-1}^{gnss}=\begin{bmatrix}1 & 0 & \Delta t\\ 0 & 1 & \Delta t\\ 0 & 0 & 1\end{bmatrix} \tag{24}$$

where $\boldsymbol{O}$ refers to the zero matrix.

D. Pedestrian Motion Constraint

When the pedestrian walks under normal conditions, it is assumed that the lateral and vertical velocities in the human-frame (h-frame, the origin is set at the shoulder and the X-axis is parallel to the walking direction) are equal to 0 [37]. When a step detected, the pedestrian velocity in the h-frame can be written as:

$$\tilde{\boldsymbol{v}}^h=[\,(\kappa+\delta\kappa)SL/\Delta t \quad 0 \quad 0\,]^T+\boldsymbol{\varepsilon}_v \tag{25}$$

where SL is the step length; Δt is the time interval between two adjacent steps; $\boldsymbol{\varepsilon}_v$ is the observation noise.

Then, the predicted velocity in the h-frame from INS can be expressed as:

$$\begin{aligned}\hat{\boldsymbol{v}}^h=&\boldsymbol{v}^h+\boldsymbol{C}_b^h\boldsymbol{C}_n^b\delta\boldsymbol{v}^n-\boldsymbol{C}_b^h\boldsymbol{C}_n^b(\boldsymbol{v}^n\times)\boldsymbol{\psi}\\&-\boldsymbol{C}_b^h(\boldsymbol{l}^b\times)\delta\boldsymbol{b}_g+\boldsymbol{C}_b^h(\boldsymbol{\omega}^b\times)\delta\boldsymbol{l}^b\end{aligned} \tag{26}$$

where $\boldsymbol{v}^h=\boldsymbol{C}_b^h\boldsymbol{C}_n^b\boldsymbol{v}^n+\boldsymbol{C}_b^h(\boldsymbol{\omega}^b\times)\boldsymbol{l}^b$; $\boldsymbol{C}_b^h$ is the transformation matrix from the b-frame to the h-frame. The mounting angle in heading is the most important element to calculate $\boldsymbol{C}_b^h$. In general, the principal direction of arm swinging is consistent with the walking direction, so the principal component analysis (PCA) method is employed to obtain $\boldsymbol{C}_b^h$ [38]. The pedestrian heading mentioned in (2) can be expressed as:

$$\varphi=\psi_{INS}-\psi_{mount} \tag{27}$$

where ψ_{INS} is the sensor heading provided by INS mechanization; ψ_{mount} is the mounting angle estimated via PCA. Finally, the observation equation is given as:

$$\begin{aligned}\delta\boldsymbol{z}_v=&\hat{\boldsymbol{v}}^h-\tilde{\boldsymbol{v}}^h\\=&\ \boldsymbol{C}_b^h\boldsymbol{C}_n^b\delta\boldsymbol{v}^n-\boldsymbol{C}_b^h\boldsymbol{C}_n^b(\boldsymbol{v}^n\times)\boldsymbol{\psi}-\boldsymbol{C}_b^h(\boldsymbol{l}^b\times)\delta\boldsymbol{b}_g\\&+\boldsymbol{C}_b^h(\boldsymbol{\omega}^b\times)\delta\boldsymbol{l}^b-\boldsymbol{v}_{step}\delta\kappa+\boldsymbol{\varepsilon}_v\end{aligned} \tag{28}$$

where $\boldsymbol{v}_{step}=[\,SL/\Delta t \quad 0 \quad 0\,]^T$.

E. Tightly-coupled GNSS/INS Integration

In this paper, single-frequency pseudorange and Doppler observations are used. When the satellite is identified as unreliable via the spatial consistency check, it no longer participates in the calculation. Utilizing the position provided by INS mechanization, the observation equations can be written as:

$$\begin{cases}\bar{\rho}=\rho_{INS}-\boldsymbol{los}_{INS}^e\cdot\delta\boldsymbol{r}^e+c\delta t_r+\varepsilon_P\\ \bar{\dot{\rho}}=\boldsymbol{los}_{INS}^e\cdot(\boldsymbol{v}_r^e-\boldsymbol{v}_s^e)+c\dot{\delta}t_r+\varepsilon_{\dot{P}}\end{cases} \tag{29}$$

where $\bar{\rho}$ is the pseudorange observations that eliminates satellite clock bias and atmospheric effects; $\bar{\dot{\rho}}$ is the pseudorange rate derived from Doppler observation, and the satellite clock drift is eliminated; the superscript e denotes the earth-centered-earth-fixed (ECEF) coordinate system (e-frame); $\rho_{INS}=\|\boldsymbol{r}_{INS}^e-\boldsymbol{r}_s^e\|$ is the distance from satellite position $\boldsymbol{r}_s^e$ to INS position $\boldsymbol{r}_{INS}^e$; $\delta\boldsymbol{r}^e$, $\boldsymbol{v}_r^e$, and $\boldsymbol{v}_s^e$ denote the position error vector, velocity of receiver and satellite in the e-frame, respectively; $c\delta t_r$ and $c\dot{\delta}t_r$ are the clock bias (in meter) and clock drift (in meter per second), respectively; ε_P and $\varepsilon_{\dot{P}}$ are the measurement errors; $\boldsymbol{los}_{INS}^e$ is the LOS unit vector from satellite to INS position in the e-frame.

Then, the predicted pseudorange and pseudorange rate from INS can be expressed as:

$$\begin{cases}\hat{\rho}=\rho_{INS}\\ \hat{\dot{\rho}}=\boldsymbol{los}_{INS}^e\cdot(\boldsymbol{v}_{INS}^e-\boldsymbol{v}_s^e)\end{cases} \tag{30}$$

where $\boldsymbol{v}_{INS}^e=\boldsymbol{v}_r^e+\delta\boldsymbol{v}^e$ is the INS velocity. Finally, the observation equation is given as:

$$\begin{cases}\delta z_P=\hat{\rho}-\bar{\rho}=\boldsymbol{los}_{INS}^e\cdot\delta\boldsymbol{r}^e-c\delta t_r+\varepsilon_P\\ \delta z_{\dot{P}}=\hat{\dot{\rho}}-\bar{\dot{\rho}}=\boldsymbol{los}_{INS}^e\cdot\delta\boldsymbol{v}^e-c\dot{\delta}t_r+\varepsilon_{\dot{P}}\end{cases} \tag{31}$$

where $\delta\boldsymbol{r}^e=\boldsymbol{C}_n^e\delta\boldsymbol{r}^n$ and $\delta\boldsymbol{v}^e=\boldsymbol{C}_n^e\delta\boldsymbol{v}^n$; $\boldsymbol{C}_n^e$ denotes the transformation matrix from the n-frame to the e-frame.

F. Weight Functions

To address GNSS outliers, RKF is one of the classical methods that has been widely used. Generally, a weight function is employed to suppress gross errors and enhance the positioning robustness. In this paper, the Institute of Geodesy and Geophysics III (IGG III) weight function is used [19]:

$$\gamma_i=\begin{cases}1 & ,v_i\leqslant c_0\\ \dfrac{c_0}{v_i}\times\left(\dfrac{c_1-v_i}{c_1-c_0}\right)^2 & ,c_0<v_i\leqslant c_1\\ 10^{-6} & ,v_i>c_1\end{cases} \tag{32}$$

where γ_i is the coefficient that scales the measurement covariance matrix; c_0 and c_1 are two thresholds with experienced values; v_i is the standardized innovation value.

However, the weight function is typically effective when mitigating abrupt faults. In GNSS/INS integration, the detection of SGEs requires additional consideration. To address this issue, the enhanced AIME algorithm [24], as

previously introduced, is adopted here. This algorithm utilizes multi-epoch innovation vectors and their covariance matrices to construct test statistics. For a given satellite, the test statistic T_j can be formulated as follows:

$$T_j = r_{avg,j}^T \cdot V_{avg,j}^{-1} \cdot r_{avg,j} \tag{33}$$

$$\begin{cases} V_{avg,j}^{-1} = \sum_{i=k-l+1}^{k} (S_i^j)^{-1} \\ r_{avg,j} = (V_{avg,j}^{-1})^{-1} \sum_{i=k-l+1}^{k} (S_i^j)^{-1} \cdot r_i^j \end{cases} \tag{34}$$

where r_i^j is the innovation value; l is the length of the sliding window; S_i^j is the principal diagonal element of the covariance matrix for the *j*-th satellite in the *i*-th epoch, and the covariance matrix is expressed as:

$$\boldsymbol{V}_i = \boldsymbol{H}_i \boldsymbol{P}_i^- \boldsymbol{H}_i^T + \boldsymbol{R}_i \tag{35}$$

where $\boldsymbol{H}_i$ is the measurement matrix; $\boldsymbol{P}_i^-$ is the covariance matrix for the predicted state vector; $\boldsymbol{R}_i$ is the measurement covariance matrix. When T_j exceeds the predefined threshold, this observation is considered to be faulty. More detailed descriptions can be found in [24].

IV. Test Description

To validate the performance of the proposed algorithm, nine sets of test data were collected across three typical urban scenarios, and the test trajectories are designed as shown in Fig. 3. Scenario1 (S1) is a typical avenue environment, partially obstructed by high-rise buildings. Scenario2 (S2) is heavily surrounded by high-rise buildings, resulting in severe GNSS signal obstruction. Scenario3 (S3) is a typical shopping mall environment, where approximately half of the sky is obstructed. S3 contains numerous glass walls, which introduce significant multipath effects and NLOS receptions. In this paper, three datasets were collected for each scenario, with each dataset containing about 15–20 minutes of valid data.

In the complex urban environments shown in Fig. 3, GNSS-based systems alone cannot provide stable and reliable reference results. Thus, the ground truth was obtained by using a handheld 3D laser scanner (Fig. 4a). To obtain the absolute coordinates, three high-precision GNSS reference points were first measured under good observation conditions. Then, relative positions were acquired using the 3D laser scanner. When passing through a reference point, the corresponding time and relative coordinates were recorded. Finally, absolute positions were derived through translation and rotation alignment. In addition, since wrist-worn devices such as smartwatches and wristbands are gaining popularity and have emerged as viable alternatives for implementing LBS [39], related data were collected in wrist-worn mode, as shown in Fig. 4b. The GNSS observations and IMU measurements were collected by INS-Probe, an integrated navigation module consisting of u-blox F9P and TDK ICM-20602.

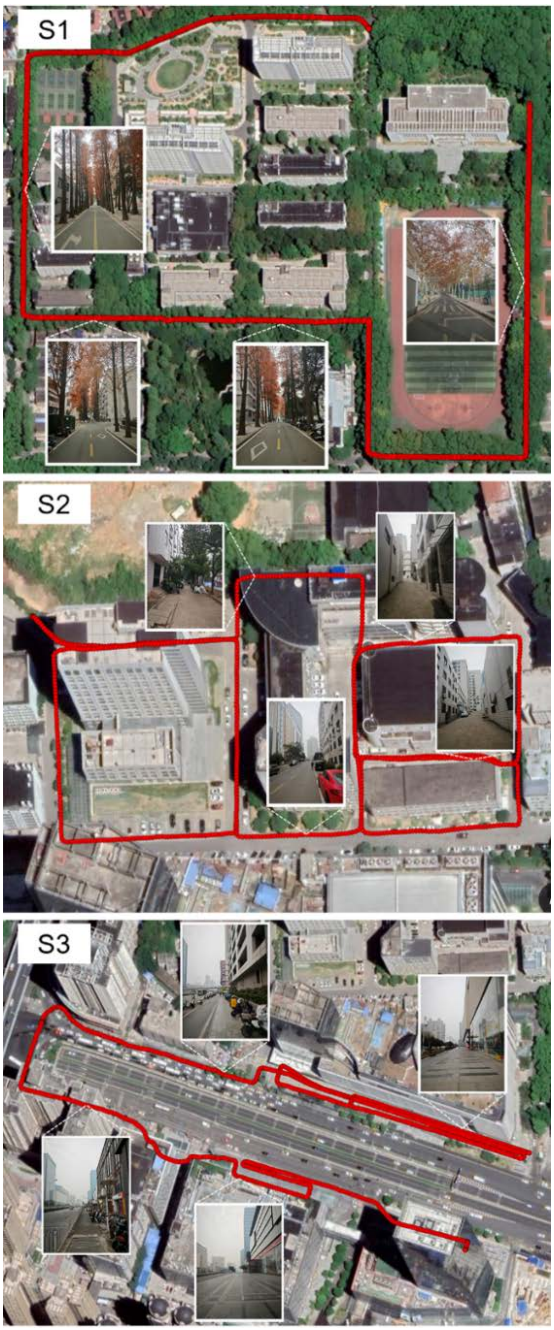

Fig. 3. Surrounding environment and test trajectories for performance evaluation.

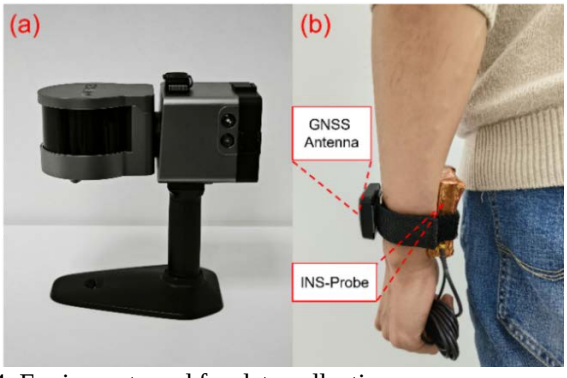

Fig. 4. Equipment used for data collection.

V. Test Results

For performance evaluation, five positioning strategies are compared, as detailed in Table I. The horizontal positioning trajectories of the five methods in three scenarios are shown in Fig. 5. From SPP results, it can be observed that S1 yields the best positioning performance, as the avenue environment imposes minimal obstruction and results in limited degradation of positioning accuracy. In contrast, S2 is heavily surrounded by high-rise buildings, and the positioning performance is significantly degraded due to severe signal obstruction. Moreover, S3 represents a typical urban environment, and positioning results in this scenario are notably affected by multipath effects and NLOS receptions. In particular, case2 within S3 demonstrates especially poor performance. The primary factor contributing to this degradation is the orientation of the GNSS antenna during data collection. In case1 and case3, the antenna predominantly faced the urban road (i.e., the open sky). However, in case2, the antenna was mostly positioned between the high-rise buildings and human body, which causes further satellite obstruction and leads to a substantial deterioration in positioning accuracy.

TABLE I
Description for the Positioning Solutions

Solutions	Description
SPP	Positioning results provided by u-blox F9P
OPT	Positioning results provided by the proposed optimization algorithm, i.e., equation (15)
TC	Tightly-coupled GNSS/INS integration with robust estimation, i.e., equation (32)
AIME-TC	TC enhanced by AIME, i.e., equation (33)
PA-TC	TC enhanced by the proposed algorithm, i.e., equation (18)

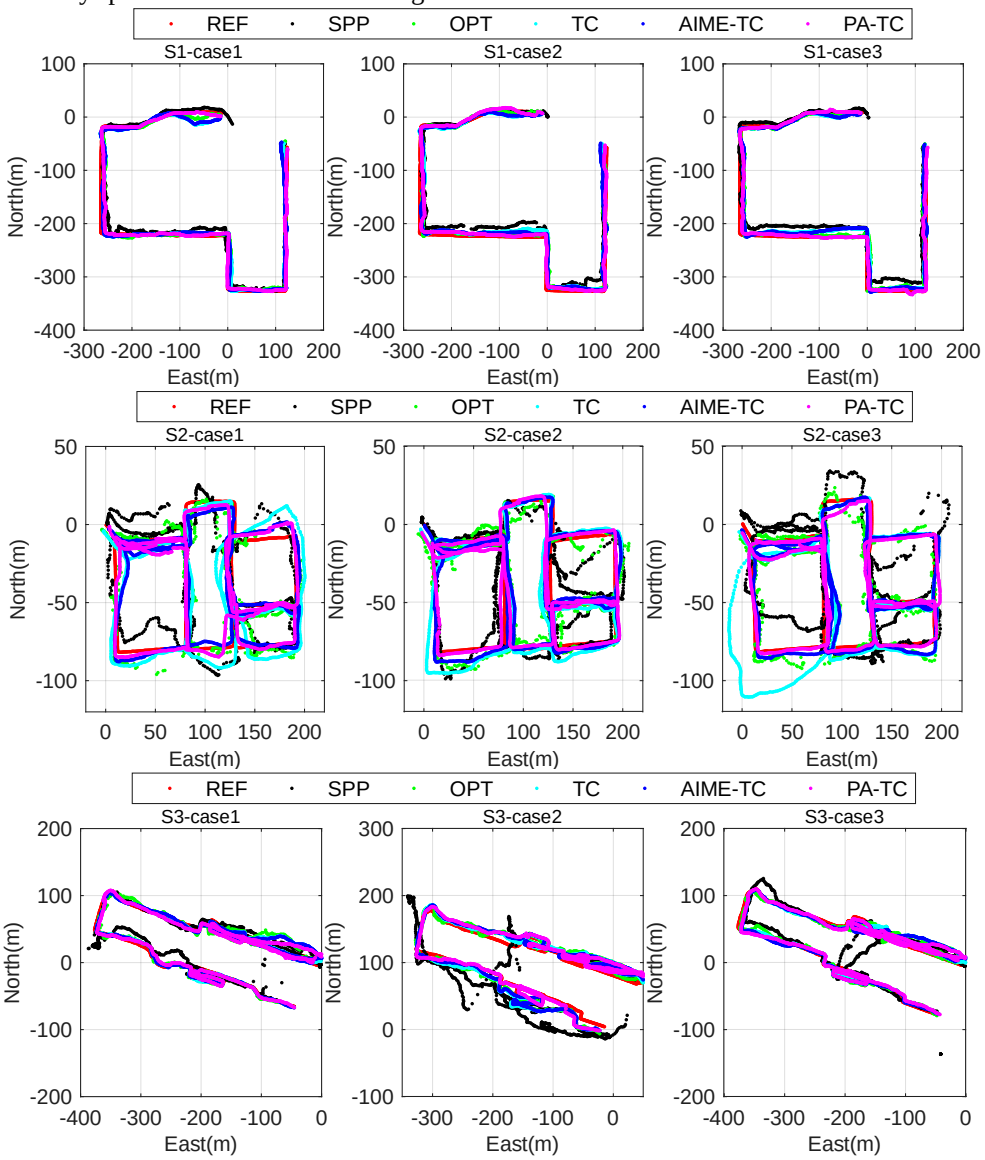

Fig. 5. Horizontal positioning trajectories of the five methods in three scenarios.

TABLE II
STATISTICAL RESULTS OF HORIZONTAL POSITION ERRORS FOR THE FIVE METHODS (UNIT: M)

		SPP			OPT			TC			AIME-TC			PA-TC		
		RMS	%68	%95	RMS	%68	%95	RMS	%68	%95	RMS	%68	%95	RMS	%68	%95
S1	case1	9.84	10.32	18.42	5.81	6.27	9.84	7.13	6.08	14.73	6.78	5.62	14.86	3.98	3.94	7.45
	case2	13.37	14.11	26.46	6.11	6.59	9.36	7.51	7.94	11.49	6.62	7.09	9.98	4.84	5.42	7.91
	case3	14.65	18.33	23.13	6.19	6.54	10.45	7.71	7.98	14.65	7.65	7.56	15.45	3.63	3.92	6.35
S2	case1	13.02	12.33	26.15	7.09	7.11	12.31	8.35	8.80	15.17	5.12	5.59	8.55	5.37	5.51	10.84
	case2	10.38	9.55	20.42	6.66	6.48	12.66	6.33	5.63	12.60	4.35	4.02	8.20	4.81	5.19	8.63
	case3	11.74	11.15	22.48	7.36	7.35	12.31	11.90	7.44	31.60	5.12	4.79	9.14	4.55	4.25	9.74
S3	case1	16.41	10.92	35.22	8.00	5.83	19.91	7.03	4.67	18.94	6.86	4.92	18.55	5.84	5.10	13.52
	case2	57.92	57.26	109.98	10.88	11.84	19.68	10.70	10.88	19.23	10.37	11.01	18.31	8.03	7.01	17.34
	case3	19.84	8.39	30.57	7.29	5.82	16.96	6.31	3.80	17.07	6.01	3.58	16.81	4.45	2.96	10.13
Mean		18.57	16.93	34.76	7.26	7.09	13.72	8.11	7.02	17.27	6.54	6.02	13.32	5.05	4.81	10.21

Additionally, compared with SPP, the other four methods demonstrate satisfactory performance in most tests. However, it is found that the TC results exhibit noticeable trajectory drift in certain areas (e.g., case3 within S2). This drift primarily manifests as a gradual deviation accumulating over time. In comparison, the trajectory drift observed in the AIME-TC results is significantly suppressed, which indicates that the employed AIME algorithm is effective in detecting and mitigating SGEs.

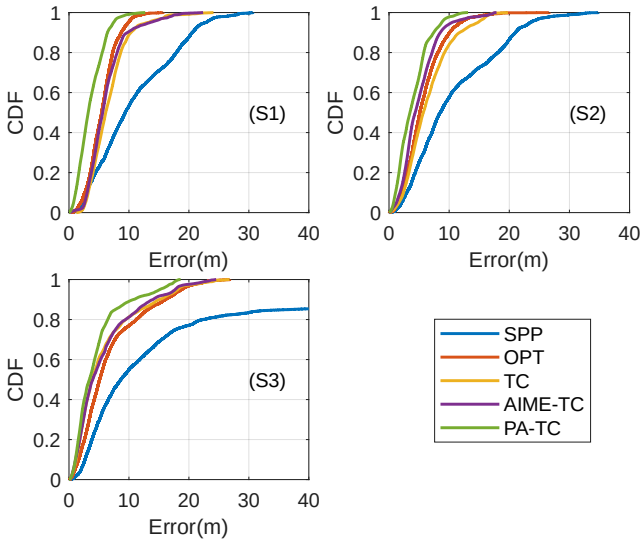

Fig. 6. The CDF of SPP, OPT, TC, AIME-TC, and PA-TC in three scenarios.

Fig. 6 shows the cumulative distribution function (CDF) of the five solutions in nine tests. The root mean square (RMS), 68%, and 95% of the horizontal position errors for each method are summarized in Table II. The average values of the three statistics in horizontal position errors are 18.57 m, 16.93 m, and 34.76 m for SPP; 7.26 m, 7.09 m, and 13.72 m for OPT; 8.11 m, 7.02 m, and 17.27 m for TC; 6.54 m, 6.02 m, and 13.32 m for AIME-TC; 5.05 m, 4.81 m, and 10.21 m for PA-TC. The statistical results clearly demonstrate that the TC-based method significantly outperforms GNSS SPP, highlighting the advantages of GNSS/INS integration for navigation applications in urban environments.

TABLE III
AVERAGE SATELLITE NUMBER OF TOTAL AND USED IN THREE SCENARIOS FOR THE PROPOSED METHOD

	S1		S2		S3	
	Total	Used	Total	Used	Total	Used
case1	15.6	3.9	9.0	2.4	12.9	4.8
case2	13.8	4.0	10.9	3.4	11.4	3.1
case3	15.6	3.4	8.4	2.3	15.2	4.7
Mean	15.0	3.8	9.4	2.7	13.2	4.2

In addition, the optimization algorithm performs slightly better than the TC method but worse than the AIME-TC and PA-TC methods. Although a cost function has been introduced to mitigate the influence of GNSS outliers, such errors cannot be completely eliminated. Moreover, the optimization problem is solved using the classical Gauss-Newton method, which imposes certain requirements on the accuracy of the initial guess. If the initial state vector is inaccurate, the algorithm may converge to a local optimum. As mentioned previously, GNC has been adopted in FGO-based algorithm. This approach follows a coarse-to-fine strategy, reducing sensitivity to initial values and enhancing robustness against GNSS outliers. Therefore, more investigations should be conducted

by using more advanced methodologies to further improve the performance of the proposed optimization algorithm.

By integrating the AIME algorithm, SGEs can be effectively detected and mitigated, resulting in higher positioning accuracy. Notably, the proposed method delivers the best performance, which achieves approximately 41% and 23% of improvement in horizontal positioning accuracy (95%) compared to the regular TC method and AIME-TC method, respectively. The improvement is primarily attributed to the adoption of a more stringent quality control strategy, namely, a satellite is considered to be fault-free only if it maintains favorable observation conditions throughout the entire sliding window. Table III presents the average number of satellites observed in each case, as well as the average number of satellites retained after applying the proposed method. Since the employed equipment records observations only from GPS, BDS, and QZSS, the average number of visible satellites is approximately 12.5. The number of visible satellites in S2 is obviously lower than that in S1 and S3, which is consistent with the surrounding environment shown in Fig. 3. After applying the proposed method, the average number of retained satellites decreases to approximately 3.6, which indicates that most faulty satellites can be excluded and explains the reasons for the performance improvement.

VI. Discussion

As shown in Fig. 6 and Table II, the proposed method achieves the best positioning performance among all evaluated approaches. Nevertheless, several aspects of the proposed algorithm merit further discussions.

TABLE IV
Duration for Each Test and the Valid Positioning Time for SPP and OPT (unit: s)

	S1			S2			S3		
	Duration	SPP	OPT	Duration	SPP	OPT	Duration	SPP	OPT
case1	910	908	891	897	894	720	1077	1068	948
case2	951	949	932	892	889	779	1027	1024	960
case3	914	914	898	846	837	712	1118	1117	1040
Mean	925.0	923.7	907.0	878.3	873.3	737.0	1074.0	1069.7	982.7

First, the state vector of the proposed optimization algorithm includes seven parameters that need to be estimated, which implies that a sufficient number of visible satellites within the sliding window is necessary. Table IV summarizes the data collection duration for each case across the three scenarios, along with the number of positioning results provided by SPP and OPT. It is found that OPT in S2 demonstrates the worst performance, with approximately 16% of results failing to converge. As illustrated in Table III, the average number of visible satellites in S2 is approximately 9.4, which is obviously lower than that in S1 and S3. Therefore, environmental factors are the main cause of this degradation. In instances where the optimization algorithm fails to converge, the proposed method automatically falls back to the conventional RKF. Nevertheless, such non-convergence events are relatively rare and constitute only a small portion of the overall dataset. In more extreme cases, GNSS signals may be completely blocked in certain areas, but the GNSS/INS integrated system can still work properly by using the pedestrian motion constraint, which further demonstrates the advantages of the proposed method in positioning integrity.

Second, the size of the sliding window is also a critical factor influencing positioning performance. On the one hand, if the window size is too short, some errors cannot be effectively identified. For example, variations of SGEs are typically small and may not be detected within a short time window using (18). On the other hand, as time progresses, the accuracy of the PDR trajectory cannot be guaranteed. Moreover, if the window size is too long, it becomes increasingly challenging for one satellite to maintain favorable observation conditions in complex urban environments, causing most satellites are discarded. As the number of usable satellites decreases significantly, positioning performance will also decrease to a certain extent. The average horizontal position errors for the proposed method with different window size are presented in Table V. It can be observed that both shorter and longer windows lead to performance degradation. Finally, 20-second window size is adopted in this paper.

TABLE V
Average Horizontal Position Errors for the Proposed Methods with Different Window Size (unit: m)

Window Size	RMS	68%	95%
10s	6.94	6.09	14.04
15s	5.42	5.22	10.97
20s	5.05	4.81	10.21
25s	8.28	6.18	17.37
30s	21.40	20.56	37.95

Third, the 20-second window also has inherent limitations. Since the pedestrian moves in a slow velocity, multipath effects or NLOS reflections may remain relatively stable within the sliding window. As a result, the spatial consistency

check may be ineffective, and Fig. 7 illustrates this phenomenon. In Fig. 7, the double-differenced (DD) pseudorange residuals of case1 within S3 are demonstrated. The red dots represent the DD residuals for all satellites, while the blue dots correspond to that of the retained satellites. It is observed that the proposed method effectively filters out the majority of GNSS outliers. However, fewer anomalies still exist, which are highlighted by the black circles. This issue is primarily attributed to the ineffectiveness of the spatial consistency check, but such instances are relatively rare across the entire dataset. Additionally, a period of missing results is highlighted with a green circle in Fig. 7. During this time, the tester remained stationary while waiting for the traffic light, so no steps were detected. In the sliding window, if the number of detected steps or the length of PDR trajectory falls below the certain thresholds, the optimized results will not be obtained.

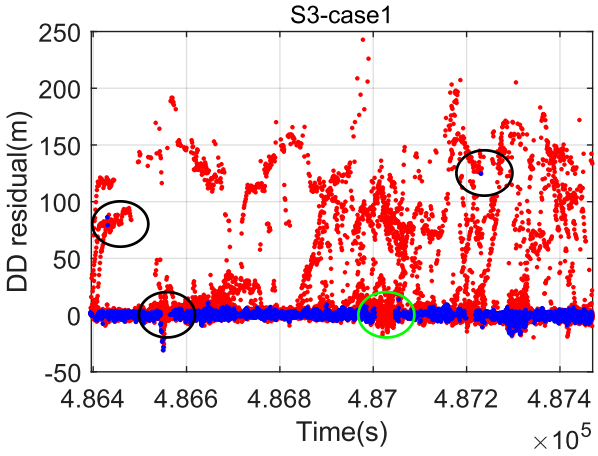

Fig. 7. Double-differenced pseudorange residuals for all satellites (red dot) and the retained satellites (blue dot) in case1 of S3.

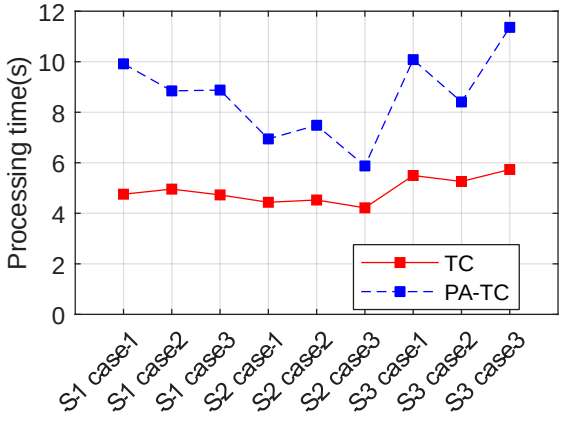

Fig. 8. Processing time of the conventional RKF and the proposed method.

Finally, the processing time of the conventional RKF and the proposed method is shown in Fig. 8, and the duration statistics for each test are summarized in Table IV. On a laptop, the average processing time of the conventional RKF is approximately 4.9 s. After incorporating the optimization algorithm, the average processing time increases to 8.6 s, which does not represent a significant increase. The proposed method improves positioning accuracy while maintaining computational efficiency, making it suitable for real-time operation on wearable devices such as smartwatches.

VII. Conclusion

This paper proposes a robust GNSS/INS integrated system for pedestrian navigation in urban environments based on spatial consistency check. Compared to the classical RKF, two additional steps are introduced. First, an optimization algorithm is employed to process the PDR trajectory and multi-epoch GNSS observations. Then, the optimized results are used for GNSS outlier detections through a spatial consistency check. On the one hand, the proposed method combines the advantages of both KF-based and optimization-based approaches. On the other hand, the optimization problem defined in this paper only requires several parameters to be estimated, resulting in lower computational load. It makes the proposed method well-suited for implementation on smart devices and provides a novel solution for pedestrian navigation in complex urban environments.

To validate the performance of the proposed method, nine sets of test data were collected covering three typical urban scenarios. To demonstrate the superiority of the proposed method, five different positioning solutions are evaluated. The mean 95% position error of the commercial u-blox module is 34.76 m, which is the worst among other methods. In addition, that of the optimization algorithm is 13.72 m, which performs slightly better than the conventional RKF (17.27 m). Moreover, the AIME enhanced method is capable of detecting SGEs, which effectively suppresses trajectory drift and improves the horizontal positioning accuracy to 13.32 m (95%). The proposed method employs a more rigorous quality control strategy and delivers the best performance, achieving the mean 95% of 10.21 m, which represents an improvement of approximately 41% and 23% compared to the conventional RKF and AIME enhanced method, respectively.

For future works, three points might be considered. First, more advanced strategies could be integrated into the optimization algorithm to further enhance its robustness. It is also worth comparing the proposed method with the sliding-window-based FGO approach to evaluate its effectiveness in GNSS outlier detection and computational load. Second, the performance of the proposed algorithm under different motion states and usage conditions should be further investigated, particularly in scenarios where the PDR performance degrades. Third, the proposed solution could be implemented on commercial devices, such as smartphone and smartwatch.

References

[1] H. Jiang, J. Li, P. Zhao, F. Zeng, Z. Xiao, and A. Iyengar, “Location privacy-preserving mechanisms in location-based services: A comprehensive survey,” *ACM Comput. Surv.*, vol. 54, no. 1, pp. 1–36, Jan. 2021.

[2] F. Zangenehnejad and Y. Gao, "GNSS smartphones positioning: Advances, challenges, opportunities, and future perspectives," *Satell. Navig*, vol. 2, no. 1, pp. 1–23, Nov. 2021.

[3] P. S. Farahsari, A. Farahzadi, J. Rezazadeh and A. Bagheri, "A survey on indoor positioning systems for IoT-based applications," *IEEE Internet Things J.*, vol. 9, no. 10, pp. 7680–7699, May 2022.

[4] Y. Wu, H. Zhu, Q. Du, and S. Tang, "A survey of the research status of pedestrian dead reckoning systems based on inertial sensors," *Int. J. Autom. Comput.*, vol. 16, no. 1, pp. 65–83, Feb. 2019.

[5] R. Sun, J. Wang, Q. Cheng, Y. Mao, and W. Y. Ochieng, "A new IMU-aided multiple GNSS fault detection and exclusion algorithm for integrated navigation in urban environments," *GPS Solut.*, vol. 25, no. 4, pp. 1–17, Oct. 2021.

[6] J. Zidan, E. I. Adegoke, E. Kampert, S. A. Birrell, C. R. Ford and M. D. Higgins, "GNSS vulnerabilities and existing solutions: A review of the literature," *IEEE Access*, vol. 9, pp. 153960–153976, Feb. 2021.

[7] R. M. Kalafus and G. Y. Chin, "Performance measures of receiver-autonomous GPS integrity monitoring," in *Proceedings of the 1988 National Technical Meeting of The Institute of Navigation*, Jan. 1988, pp. 223–229.

[8] N. Zhu, J. Marais, D. Bétaille, and M. Berbineau, "GNSS position integrity in urban environments: A review of literature," *IEEE Trans. Intell. Transport. Syst*, vol. 19, no. 9, pp. 2762–2778, Sep. 2018.

[9] J. Blanch, T. Walter, and P. Enge, "RAIM with optimal integrity and continuity allocations under multiple failures," *IEEE Trans. Aerosp. Electron. Syst.*, vol. 46, no. 3, pp. 1235–1247, Jul. 2010.

[10] Y. Yang and J. Xu, "GNSS receiver autonomous integrity monitoring (RAIM) algorithm based on robust estimation," *Geodesy and Geodynamics*, vol. 7, no. 2, pp. 117–123, Mar. 2016.

[11] Y. Wen, W. Dai, W. Yu, and L. Pan, "Mitigation of multiple outliers using consistency checking for GNSS standard point positioning in urban areas," *Advances in Space Research*, vol. 73, no. 3, pp. 1721–1733, Feb. 2024.

[12] W. Wen, G. Zhang, and L.-T. Hsu, "GNSS outlier mitigation via graduated non-convexity factor graph optimization," *IEEE Trans. Veh. Technol.*, vol. 71, no. 1, pp. 297–310, Jan. 2022.

[13] L. Wang, P. D. Groves, and M. K. Ziebart, "GNSS shadow matching: Improving urban positioning accuracy using a 3D city model with optimized visibility scoring scheme," *J Inst Navig*, vol. 60, no. 3, pp. 195–207, Sep. 2013.

[14] X. Bai, W. Wen, and L.-T. Hsu, "Using sky-pointing fish-eye camera and LiDAR to aid GNSS single-point positioning in urban canyons," *IET Intell. Transp. Syst.*, vol. 14, no. 8, pp. 908–914, May 2020.

[15] A. El-Mowafy, B. Xu, and L.-T. Hsu, "Integrity monitoring using multi-GNSS pseudorange observations in the urban environment combining ARAIM and 3D city models," *Journal of Spatial Science*, vol. 67, no. 1, pp. 91–110, Jan. 2022.

[16] D. Weng, W. Chen, M. Ding, S. Liu, and J. Wang, "Sidewalk matching: A smartphone-based GNSS positioning technique for pedestrians in urban canyons," *Satell. Navig.*, vol. 6, no. 1, pp. 1–15, Dec. 2025.

[17] H. Liu, Z. Gao, L. Wang, Q. Xu and C. Yang, "Reliable positioning model of smartphone sensors and user motions tightly enhanced PDR," *IEEE Internet Things J.*, vol. 11, no. 19, pp. 30925–30938, Oct. 2024.

[18] X. Niu, Y. Dai, T. Liu, Q. Chen, and Q. Zhang, "Feature-based GNSS positioning error consistency optimization for GNSS/INS integrated system," *GPS Solut.*, vol. 27, no. 2, pp. 1–14, Mar. 2023.

[19] Y. Yang, W. Gao, and X. Zhang, "Robust Kalman filtering with constraints: A case study for integrated navigation," *J Geod*, vol. 84, no. 6, pp. 373–381, Jun. 2010.

[20] Z. Yu, Q. Zhang, K. Yu, and N. Zheng, "A state-domain robust chi-square test method for GNSS/INS integrated navigation," *Journal of Sensors*, vol. 2021, pp. 1–8, Oct. 2021.

[21] Q. Zhang, H. Lin, L. Ding, Q. Chen, T. Zhang, and X. Niu, "RANSAC-based fault detection and exclusion algorithm for single-difference tightly coupled GNSS/INS integration," *IEEE Trans. Intell. Veh.*, vol. 9, no. 2, pp. 3986–3997, Feb. 2024.

[22] H. Jing, Y. Gao, S. Shahbeigi, and M. Dianati, "Integrity monitoring of GNSS/INS based positioning systems for autonomous vehicles: State-of-the-art and open challenges," *IEEE Trans. Intell. Transport. Syst.*, vol. 23, no. 9, pp. 14166–14187, Sep. 2022.

[23] U. I. Bhatti, W. Y. Ochieng, and S. Feng, "Integrity of an integrated GPS/INS system in the presence of slowly growing errors. Part I: A critical review," *GPS Solut.*, vol. 11, no. 3, pp. 173–181, Jul. 2007.

[24] H. Jiang, D. Yan, J. Wang, and J. Yin, "Innovation-based Kalman filter fault detection and exclusion method against all-source faults for tightly coupled GNSS/INS/Vision integration," *GPS Solut.*, vol. 28, no. 3, pp. 1–17, Jul. 2024.

[25] N. Sunderhauf, M. Obst, G. Wanielik, and P. Protzel, "Multipath mitigation in GNSS-based localization using robust optimization," in *2012 IEEE Intelligent Vehicles Symposium*, Jun. 2012, pp. 784–789.

[26] W. Wen, T. Pfeifer, X. Bai, and L.-T. Hsu, "Factor graph optimization for GNSS/INS integration: A comparison with the extended Kalman filter," *Navigation*, vol. 68, no. 2, pp. 315–331, Jun. 2021.

[27] H. Yang, P. Antonante, V. Tzoumas, and L. Carlone, "Graduated non-convexity for robust spatial perception: From non-minimal solvers to global outlier rejection," *IEEE Rob. Autom. Lett.*, vol. 5, no. 2, pp. 1127–1134, Apr. 2020.

[28] C. Jiang, Y. Chen, C. Chen, J. Jia, H. Sun, T. Wang, and J. Hyyppä, "Smartphone PDR/GNSS integration via factor graph optimization for pedestrian navigation," *IEEE Trans. Instrum. Meas.*, vol. 71, pp. 1–12, Jun. 2022.

[29] Y. Zhong, W. Wen, and L.-T. Hsu, "Trajectory smoothing using GNSS/PDR integration via factor graph optimization in urban canyons," *IEEE Internet Things J.*, vol. 11, no. 14, pp. 25425–25439, Jul. 2024.

[30] C. Jiang, Y. Chen, C. Chen, and J. Hyyppä, "Walking gaits aided mobile GNSS for pedestrian navigation in urban areas," *IEEE Internet Things J.*, vol. 11, no. 5, pp. 8499–8510, Mar. 2024.

[31] J. Bi, J. Wang, B. Yu, G. Yao, Y. Wang, H. Cao, L. Huang, and H. Xing, "Precise step counting algorithm for pedestrians using ultra-low-cost foot-mounted accelerometer," *Eng. Appl. Artif. Intell.*, vol. 150, pp. 1–14, Jun. 2025.

[32] C. Jiang, Y. Chen, C. Chen, J. Jia, H. Sun, T. Wang, and J. Hyyppä, "Implementation and performance analysis of the PDR/GNSS integration on a smartphone," *GPS Solut.*, vol. 26, no. 3, pp. 1–9, Jul. 2022.

[33] R. Chen, L. Pei, and Y. Chen, "A smart phone based PDR solution for indoor navigation," in *Proceedings of the ION GNSS+ 2011*, Sep. 2011, pp. 1404–1408.

[34] J. Kuang, L. Ding, Y. Wang, Y. Yuan, P. Jiang, Q. Zhou, and X. Niu, "A robust INS state initialization method for vehicular GNSS/MEMS-INS integrated navigation in urban environment," *IEEE Trans. Intell. Transport. Syst.*, May 2025.

[35] L. Carlone and G. C. Calafiore, "Convex relaxations for pose graph optimization with outliers," *IEEE Rob. Autom. Lett.*, vol. 3, no. 2, pp. 1160–1167, Apr. 2018.

[36] J. Kuang, X. Niu, and X. Chen, "Robust pedestrian dead reckoning based on MEMS-IMU for smartphones," *Sensors*, vol. 18, no. 5, pp. 1–18, May 2018.

[37] J. Kuang, T. Li, and X. Niu, "Magnetometer bias insensitive magnetic field matching based on pedestrian dead reckoning for smartphone indoor positioning," *IEEE Sensors J.*, vol. 22, no. 6, pp. 4790–4799, Mar. 2022.

[38] K. Kunze, P. Lukowicz, K. Partridge, and B. Begole, "Which way am I facing: Inferring horizontal device orientation from an accelerometer signal," in *2009 International Symposium on Wearable Computers*, Sep. 2009, pp. 149–150.

[39] L. E. Diez, A. Bahillo, J. Otegui, T. Otim, "Suitability analysis of wrist-worn sensors for implementing pedestrian dead reckoning systems," *IEEE Sensors J.*, vol. 18, no. 12, pp. 5098–5114, Jun. 2018.